Nano Research
2022, 15(7): 5857–5864

ISSN 1998-0124 CN 11-5974/O4
https://doi.org/10.1007/s12274-022-4227-4

Research Article

Partially charged single-atom Ru supported on ZrO_2 nanocrystals for highly efficient ethylene hydrosilylation with triethoxysilane

Mingyan Li[1,2,§], Shu Zhao[3,§], Jing Li[2,§], Xiao Chen[4], Yongjun Ji[5] (✉), Haijun Yu[3], Dingrong Bai[1,6], Guangwen Xu[1,6] (✉), Ziyi Zhong[7,8], and Fabing Su[2,6] (✉)

[1] *Key Laboratory of Resources Chemicals and Materials (Shenyang University of Chemical Technology), Ministry of Education, Shenyang 110142, China*
[2] *State Key Laboratory of Multiphase Complex Systems, Institute of Process Engineering, Chinese Academy of Sciences, Beijing 100190, China*
[3] *Faculty of Materials and Manufacturing, Institute of Advanced Battery Materials and Devices, Beijing University of Technology, Beijing 100124, China*
[4] *Department of Chemical Engineering, Beijing Key Laboratory of Green Chemical Reaction Engineering and Technology, Tsinghua University, Beijing 100084, China*
[5] *School of Light Industry, Beijing Technology and Business University, Beijing 100048, China*
[6] *Institute of Industrial Chemistry and Energy Technology, Shenyang University of Chemical Technology, Shenyang 110142, China*
[7] *Department of Chemical Engineering, Guangdong Technion-Israel Institute of Technology (GTIIT), Shantou 515063, China*
[8] *Technion-Israel Institute of Technology (IIT), Haifa 32000, Israel*
[§] *Mingyan Li, Shu Zhao, and Jing Li contributed equally to this work.*

Received: 4 January 2022 / **Revised:** 10 February 2022 / **Accepted:** 11 February 2022

ABSTRACT

Homogeneous noble metal catalysts used in alkene hydrosilylation reactions to manufacture organosilicon compounds commercially often suffer from difficulties in catalyst recovering and recycling, undesired disproportionation reactions, and energy-intensive purification of products. Herein, we report a heterogeneous $0.5Ru^{\delta+}/ZrO_2$ catalyst with partially charged single-atom Ru (0.5 wt.% Ru) supported on commercial ZrO_2 nanocrystals synthesized by the simple impregnation method followed by H_2 reduction. When used in the ethylene hydrosilylation with triethoxysilane to produce the desired ethyltriethoxysilane, $0.5Ru^{\delta+}/ZrO_2$ showed excellent catalytic performance with the maximum Ru atom utilization and good recyclability, even superior to homogeneous catalyst ($RuCl_3 \cdot H_2O$). Structural characterizations and density functional theory calculations reveal the atomic dispersion of the active Ru species and their unique electronic properties distinct from the homogeneous catalyst. The reaction route over this catalyst is supposed to follow the typical Chalk–Harrod mechanism. This highly efficient and supported single-atom Ru catalyst has the potential to replace the current homogeneous catalyst for a greener hydrosilylation industry.

KEYWORDS

single-atom Ru, heterogeneous catalysts, hydrosilylation reaction, high performance

1 Introduction

The hydrosilylation reaction is commercially employed to manufacture organosilicon compounds by catalytic addition of Si–H bonds [1], and these products are widely used as silane coupling agents, surfactants, demolding coatings, lubricants, and adhesives [2, 3]. Currently, noble metal homogeneous catalysts, e.g., Speier catalyst (H_2PtCl_6) [4] and Karstedt catalyst (the mixture of H_2PtCl_6, C_2H_5OH, and $NaHCO_3$) [5], are commonly used in industrial hydrosilylation processes. Other homogeneous catalysts found to be effective for hydrosilylation include $Ru_3(CO)_{12}$ [6], $Ru_2C_{14}(CO)_6$ [7], $RhCl(PPh_3)_3$ [8], $RhCl(CO)(PPh_3)_2$ [8], $RhH(CO)(PPh_3)_3$ [8], and $[RhCl(CO)_2]_2$ [8], but are still mainly investigated in the laboratories. In general, these homogeneous catalysts suffer from nonrecyclable use, unwanted disproportionation reactions, inconvenient recovery of noble metal catalysts, and energy-intensive purification of products [9–11]. Therefore, heterogeneous noble metal catalysts featuring facile separation and recycling properties have been investigated for the hydrosilylation reaction [12, 13], including Pt nanoparticles supported on activated carbon and graphite [14], Pt/C nanoparticles [15], Pd-CMP-1 [16], Pt/C [17], Ru-MgO and Pt-MgO [18], and Pt nanoparticles encapsulated in a sol-gel derived porous matrix of methyltriethoxysilane [11]. However, these heterogeneous catalysts still have not come into industrial applications due to their low efficiency of atom utilization, leaching of active species, unsatisfactory catalytic performance, and limited stability. Thus, we expected to develop a catalyst system with combined advantages of the homogeneous and heterogeneous catalysts to overcome the technical barrier for the aforementioned above.

Single-atom catalysts (SACs) have high atom utilization efficiency and controllable characteristics of the active sites, being able to bridge the homogeneous and heterogeneous systems

---

Address correspondence to Yongjun Ji, 20200601@btbu.edu.cn; Guangwen Xu, gwxu@syuct.edu.cn; Fabing Su, fbsu@ipe.ac.cn

[19–21]. Indeed, some SACs have shown excellent catalytic performance comparable to or even better than homogeneous catalysts. For example, the single-atom Rh catalyst supported on nanodiamond showed excellent catalytic activity in the hydroformylation of aryl ethylene, even comparable to the homogeneous $RhCl(PPh_3)_3$ catalyst [22]. Co SACs supported on carbon nitride (CN) showed much better catalytic properties for oxidation of ethylbenzene in air than nanosized or homogenous Co catalysts [23]. The single-atom Rh catalyst supported on ZnO showed catalytic properties in the hydroformylation of alkenes comparable to the homogeneous $RhCl(PPh_3)_3$ catalyst [24]. The activity of a single-atom Ru catalyst supported on layered double hydroxide was better than that of $RuCl_3$ in a hydrogenation reaction [25]. Single-atom Pt on Fe_3O_4-SiO_2 core–shell nanoparticles exhibited excellent catalytic performance in hydrosilylation comparable to homogeneous H_2PtCl_6 catalyst [26]. Chen et al. reported that a partially charged single-atom Pt/TiO_2 catalyst exhibited remarkable activity, optimal selectivity, and excellent reusability toward anti-Markovnikov alkene hydrosilylation, much better than conventional Pt nanocatalysts [27]. A single-atom Pt/Al_2O_3 catalyst used in the hydrosilylation reaction of 1-octene and diethoxymethylsilane displayed super catalytic activity and selectivity, superior to the traditional Pt/Al_2O_3 nanocatalysts and even comparable to the commercial Karstedt catalyst [28].

The development of heterogeneous Ru SACs for the hydrosilylation reactions is highly desirable because of the much lower cost of Ru noble metal than that of Pt. Many Ru SACs have been prepared recently, including Ru/N-C [29], Ru@2H-MoS_2 [30], Ru/HZ [31], Ru/H-TiO_2 [32], Ru/UiO-66 [33], and Ru/Nb_2O_5 [34]. However, the preparation of these Ru SACs involves complicated synthetic procedures, toxic or expensive chemicals, harsh treatment conditions, and lab-made special supports; thus, they are not suitable for commercial applications. Moreover, to the best of our knowledge, there have been no reports on the use of Ru SACs in hydrosilylation, although Pt SACs have been used in this reaction [27, 28, 35].

This work reports a low-cost synthesis of a partially charged single-atom Ru catalyst supported on commercial ZrO_2 nanocrystals ($0.5Ru^{\delta+}/ZrO_2$) by the simple impregnation method followed by H_2-reduction. The obtained $0.5Ru^{\delta+}/ZrO_2$ shows excellent catalytic performance in the ethylene hydrosilylation with triethoxysilane (TES) to produce the desired ethyltriethoxysilane (ETES) (Scheme 1), even superior to the homogeneous industrial catalyst ($RuCl_3{\cdot}H_2O$) under different reaction conditions. Importantly, this heterogeneous Ru SACs with the high atom utilization efficiency can be easily recovered and recycled, with a high potential to realize a greener industrial hydrosilylation process

2 Experimental

2.1 Chemicals

All the chemicals were purchased from several Chinese companies and used directly without further processing. Ruodium(III) chloride hydrate ($RuCl_3{\cdot}H_2O$, analytical grade (AR) ≥ 44.0 wt.%) was purchased from Shanxi Kaida Chemical Co. Ltd., zirconium dioxide (ZrO_2, AR ≥ 99.9 wt.%, specific surface area: 40 m^2/g) from Zhejiang Yamei Nano Technology Co., Ltd., triethoxysilane (TES, AR ≥ 97.0 wt.%) from Chengdu Maikaxi Chemical Co., Ltd., gaseous ethylene (C_2H_4 ≥ 98.5 wt.%) from Beijing Haipu Gas Co., Ltd., methylbenzene (C_7H_8, AR, ≥ 99.5 wt.%) and ethanol (C_2H_5OH, AR ≥ 99.7 wt.%) from Sinopharm Group Chemical Reagent Co. Ltd., cerium dioxide (CeO_2), aluminum oxide (Al_2O_3), and silica (SiO_2) from Sinopharm Group Chemical Reagent Co. Ltd.

2.2 Synthesis of catalysts

First, 0.112 g $RuCl_3{\cdot}H_2O$ was dissolved in 25 mL deionized water, and then 10 g ZrO_2 was added into this solution, which was stirred at room temperature for 5 h. The obtained wet solid was then dried at 100 °C overnight and further calcined in air at 400 °C for 2 h with a heating rate of 5 °C/min. Next, the calcined sample was reduced in a tubular oven under H_2/Ar flow (50/50 vol.%, 60 mL/min) at 170 °C (5 °C/min heating rate) for 2 h. The reduced sample was pressed into tablets by adding 5 wt.% graphite powder and named $0.5Ru^{\delta+}/ZrO_2$. And the other Ru-based catalysts supported on CeO_2, Al_2O_3, and SiO_2 were synthesized following the same procedures for $0.5Ru^{\delta+}/ZrO_2$.

2.3 Characterization

Thermogravimetric (TG) analysis was performed on a TG-DTA6300 instrument at a heating rate of 10 °C/min up to 900 °C in an air flow (200 mL/min). Hydrogen temperature-programmed reduction (H_2-TPR) and temperature-programmed desorption (H_2/TPD) experiments were carried out on an automated chemisorption analyzer (Quantachrome, Chem BET pulsar TPR/TPD). For the H_2-TPR test, a 50 mg sample was put into a quartz U-tube reactor and pretreated at 150 °C for 2 h under He flow, followed by cooling to 50 °C. Afterward, the sample was heated to 900 °C (10 °C/min) under H_2/Ar flow. For H_2/TPD, a 100 mg sample was pre-reduced at 600 °C for 1 h in a 10% H_2/Ar flow and then cooled to 50 °C and saturated with H_2. After purging the physically adsorbed H_2 under Ar flow for 2 h, the sample was heated to 900 °C (10 °C/min) for H_2-TPD in Ar flow. The X-ray diffraction patterns (XRD) were recorded on a PANalytica X'Pert PRO MPD using Cu Kα radiation (λ = 1.5418 Å) at 40 kV and 40 mA and compared with the standard cards of the Joint Committee on Powder Diffraction Standards (JCPDS). The shape and microstructure of the samples were observed using a scanning electron microscope (SEM) (JSM-7800, Japan) and a field-emission transmission electron microscope (TEM) (JEM-2100F, JEOL, Japan) operated at 200 kV. The surface chemical composition was measured on a VG ESCALAB 250 X-ray photoelectron spectroscopy (XPS) instrument (Thermo Electron, UK) with a non-monochromatized Al Kα X-ray source (1,486 eV). The AC high-angle annular dark field-scanning transmission electron microscopy (HAADF-STEM) image was obtained on aberration-corrected HAADF-STEM (FEI-Titan Cubed Themis G2 300, Netherland). X-ray absorption spectroscopy (XAS) data were analyzed using the IFEFFIT package, in which energy calibration to respective metal foils and spectral normalization were performed using Athena software [36]. A cubic spline function was used to fit the background above the absorption edge. For extended X-ray absorption fine structure (EXAFS) analysis, k^3 weighting was applied to amplify the EXAFS oscillations in the mid-k region. Then, a Fourier transform process was conducted to convert data to a radial distribution (R) space with a k range at the Ru K edge. The product was analyzed by gas chromatography (GC) (7890B, Agilent, China).

2.4 Catalytic measurement

The catalytic properties of the Ru catalysts for ethylene and TES reaction were evaluated using a 100 mL stainless steel autoclave reactor with a polytetrafluoroethylene (PTFE) lining. A given amount of Ru catalyst (20–40 meshes) and 25 mL of TES were placed in the reactor. Ethylene gas (60 mL/min) was continuously fed into the reactor. The reaction system was stirred at 250 rpm under a given pressure and temperature. After a given reaction time, the reactor was cooled to room temperature, and the pressure in the reactor was released. The product liquid in the reactor was analyzed using an isocratic high-performance liquid chromatograph (Agilent 7890B) system with an Agilent 7890B standard variable wavelength ultraviolet (UV) detector and an HP-5 normal phase column. The TES conversion, ETES selectivity, and yield are calculated by the following Eqs. (1)–(3)

$$\text{TES conversion: } C_{\text{TES}}(\%) = \frac{m_{\text{TES.before}} - m_{\text{TES.after}}}{m_{\text{TES.before}}} \times 100\% \quad (1)$$

$$\text{ETES selectivity: } S_{\text{ETES}}(\%) = \frac{m_{\text{ETES}}}{m_{\text{ETES}} + m_{\text{TEOS}}} \times 100\% \quad (2)$$

$$\text{ETES yield: } Y_{\text{ETES}}(\%) = C_{\text{TES}} \times S_{\text{ETES}} \times 100\% \quad (3)$$

herein, $m_{\text{TES.before}}$ and $m_{\text{TES.after}}$ in Eq. (1) represent the mass of TES before and after the reaction, respectively, and m_{ETES} and m_{TEOS} in Eq. (2) are the mass of ETES and TEOS, respectively (in percentage; peak area calibrated with response factor).

Recycling performance of the catalysts: The solid catalyst was recovered by centrifugation and dried at 100 °C overnight after each run. Then, the recycling performance was evaluated under the same conditions.

2.5 Density functional theory (DFT) calculation

The calculations were performed using spin-polarized density functional theory (DFT) methods implemented in the Vienna *ab initio* simulation package (VASP) code [37, 38]. The projector augmented wave (PAW) method was used to describe the interactions between the ions and valence electrons [39]. The exchange–correlation interactions of valence electrons were calculated via the generalized gradient approximation (GGA) in the Perdew–Burke–Ernzerhof (PBE) form [40]. The valence orbitals of Zr (5s, 4d), Ru (4d, 5s), Si (3s, 3p), O (2s, 2p), C (2s, 2p), and H (1s) were described by plane-wave basis sets with cut-off energies of 450 eV, whereas the Brillouin zone was sampled at the Γ-point. DFT + U calculations [41, 42] with a value of $U_{\text{eff}} = 4.0$ eV for the Zr 4d state [43] were applied to correct the strong electron-correlation properties of ZrO_2. The convergence criteria for the electronic self-consistent iteration and force were set to 10^{-4} eV and 0.02 eV/Å, respectively. All transition states and pathways were computed using the climbing image nudged elastic band (CI-NEB) method to evaluate the energy barriers [44–46]. The $ZrO_2(111)$ surface was modeled by a p(2 × 2) supercell including two Zr layers, and the vacuum gap was set as ~ 15 Å. To simplify the calculation, $SiH(OMe)_3$ was used in simulation [27].

3 Results and discussion

3.1 Characterization of $0.5Ru^{\delta+}/ZrO_2$

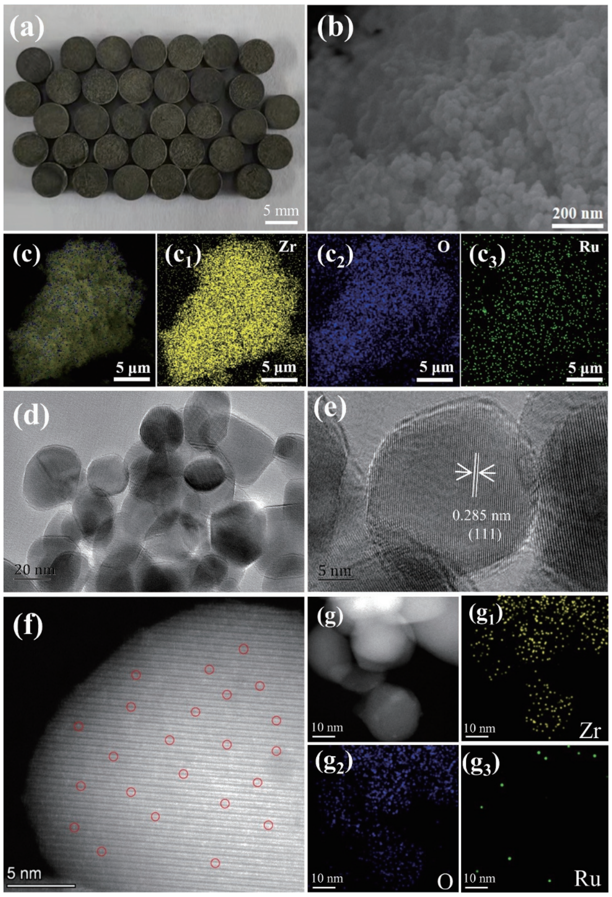

Figure 1 Structural characterizations of the $0.5Ru^{\delta+}/ZrO_2$ catalyst. (a) Photograph picture, and ((b) and (c)) SEM images: SEM-EDS elemental mapping images of (c_1) Zr, (c_2) O, and (c_3) Ru. ((d) and (e)) TEM images, and ((f) and (g)) AC HAADF-STEM image: elemental mapping images of (g_1) Zr, (g_2) O, and (g_3) Ru.

$(EtO)_3SiH + C_2H_4 = EtSi(EtO)_3 + Si(EtO)_4$ + trace other products

(TES) (ETES) (TEOS)

Scheme 1 Synthesis of ETES by Ru-catalyzed hydrosilylation reaction.

Figure 1(a) shows a photograph of the obtained $0.5Ru^{\delta+}/ZrO_2$ tablets; each has a diameter of 5 mm and a thickness of 3–4 mm. It should be mentioned that the TG curve of the $0.5Ru^{\delta+}/ZrO_2$ catalyst in the air before calcination shows a low plateau around 400 °C (Fig. S1(a) in the Electronic Supplementary Material (ESM)), thus this temperature was chosen for catalyst calcination. The H_2-TPR profile of the $0.5Ru^{\delta+}/ZrO_2$ catalyst after calcination in air at 400 °C and before the reduction in H_2/Ar (Fig. S1(b) in the ESM) shows a strong peak centered at approximately 170 °C, which is the temperature chosen for catalyst reduction. It is noted that the preparation of this catalyst does not involve complicated synthesis procedures, any toxic or expensive chemicals, and harsh treatment conditions, and thus could be easily scaled up for commercial applications. The SEM image of $0.5Ru^{\delta+}/ZrO_2$ in Fig. 1(b) shows that the catalyst consists of many ZrO_2 nanoparticles with a size of 20–30 nm, and a morphology similar to that of the pristine ZrO_2 (Fig. S2 in the ESM). The SEM-energy dispersive X-ray spectroscopy (SEM-EDS) elemental mapping analysis of $0.5Ru^{\delta+}/ZrO_2$ in Fig. 1(c) indicates the highly dispersed Ru element (Fig. 1(c_3)) on the ZrO_2 support (Figs. 1(c_1) and 1(c_2)). The TEM image in Fig. 1(d) further confirms that the particle sizes of $0.5Ru^{\delta+}/ZrO_2$ are in the range of 20–30 nm. The high-resolution transmission electron microscopy (HRTEM) image in Fig. 1(e) shows that ZrO_2 is a single crystal, and its lattice spacing measured is 0.285 nm, corresponding to the (111) crystal plane of monoclinic ZrO_2. No Ru nanoparticles or clusters are observed in Figs. 1(d) and 1(e), consistent with its XRD characterization results (Fig. S3(a) in the ESM), which do not show any diffraction peaks related to Ru species except the strong ZrO_2 characteristic peaks. The Ru dispersion on $0.5Ru^{\delta+}/ZrO_2$ is calculated to be 91.8% using its H_2-TPD profile (Fig. S3(b) in the ESM), suggesting that the highly dispersed Ru species may exist as single atoms. This conclusion is further supported by the AC HAADF-STEM image (Fig. 1(f)), in which abundant isolated bright spots marked by red circles can be assigned to Ru single atoms because of a larger atomic number of Ru than Zr, clearly verifying the atomic dispersion of Ru [47]. The elemental mapping image on $0.5Ru^{\delta+}/ZrO_2$ (Fig. 1(g)) reveals that Zr (Fig. 1(g_1)), O (Fig. 1(g_2)), and Ru (Fig. 1(g_3)) are highly dispersed, although the Ru signal seems slightly weak.

Figure 2(a) shows the XPS spectrum of Zr 3d for 0.5Ru$^{\delta+}$/ZrO$_2$. Two peaks are observed at 181.8 and 184.2 eV, assigned to the binding energies of the 3d$_{5/2}$ and 3d$_{3/2}$ electrons of Zr^{4+}, respectively [48]. In Fig. 2(b), the O 1s peaks are broad and asymmetric and can be fitted into two peaks using the Gaussian function. The peak at 530.2 eV is ascribed to the lattice oxygen in ZrO$_2$ (O$_{\rm I}$), while the peak at 531.8 eV to the surface adsorbed oxygen (O$_{\rm II}$) (active oxygen species) [49–51]. As shown in Fig. 2(c), the Ru 3p spectrum can be deconvoluted into two peaks with binding energies at 462.4 and 485.1 eV, corresponding to the 3p$_{3/2}$ and 3p$_{1/2}$ levels, respectively [30, 52]. The peak positions are between those of Ru(Ⅳ) and Ru(0), indicating that single-atom Ru is positively charged through electron transfer to ZrO$_2$, similar to the partially charged single-atom Pt/TiO$_2$ catalyst [27].

In Fig. 2(d), the XANES spectra show that the energy absorption edge and white line peak of 0.5Ru$^{\delta+}$/ZrO$_2$ are situated between the Ru foil and RuO$_2$, suggesting that the valence state of the positively charged Ru atoms in 0.5Ru$^{\delta+}$/ZrO$_2$ is between 0 and +4, which is in line with the XPS results. Figure 2(e) shows the EXAFS curve of 0.5Ru$^{\delta+}$/ZrO$_2$, with Ru foils and RuO$_2$ as reference samples. 0.5Ru$^{\delta+}$/ZrO$_2$ exhibits only one prominent peak at approximately 1.4 Å, associated with the first shell of Ru–O scattering. No reflection from the Ru–Ru contribution is observed compared with Ru foils. This result demonstrates the sole existence of atomically dispersed Ru in 0.5Ru$^{\delta+}$/ZrO$_2$, in good agreement with the above AC HAADF-STEM characterization results. Quantitative EXAFS fitting is performed (Figs. 2(f) and 2(g)), and the structural parameters of 0.5Ru$^{\delta+}$/ZrO$_2$ are listed in Table S1 in the ESM. In detail, 0.5Ru$^{\delta+}$/ZrO$_2$ shows Ru–O coordination at 2.03 ± 0.09 Å with a CN of 2.61 ± 0.3. To further reinforce this finding, we performed wavelet transform (WT) analysis of Ru EXAFS oscillations (Fig. 2(h)) [53]. As illustrated by the WT contour plots of 0.5Ru$^{\delta+}$/ZrO$_2$ [54], there is only one intensity maximum at approximately 4.1 Å^{-1} from the Ru–O contributions but without the intensity maximum near 7.9 Å^{-1}, which is indexed to the Ru–Ru path. Taking together with the AC HAADF-STEM, XANES, EXAFS, and WT analysis results, we conclude that the Ru species are atomically dispersed in 0.5Ru$^{\delta+}$/ZrO$_2$ and stabilized by O atoms; furthermore, as a result of electron transfer from Ru to ZrO$_2$, Ru atoms are partially positively charged.

3.2 Catalytic performance

We further investigated the performance of the 0.5Ru$^{\delta+}$/ZrO$_2$ catalyst in the hydrosilylation of TES with ethylene to produce ETES under different reaction conditions and compared it with the homogeneous RuCl$_3$·H$_2$O catalyst, which may lay a foundation for the use of heterogeneous Ru catalysts in industry. In the reaction temperature range of 50–80 °C, the ETES selectivity (Fig. 3(a_1)), TES conversion (Fig. 3(a_2)), and ETES yield (Fig. 3(a_3)) of

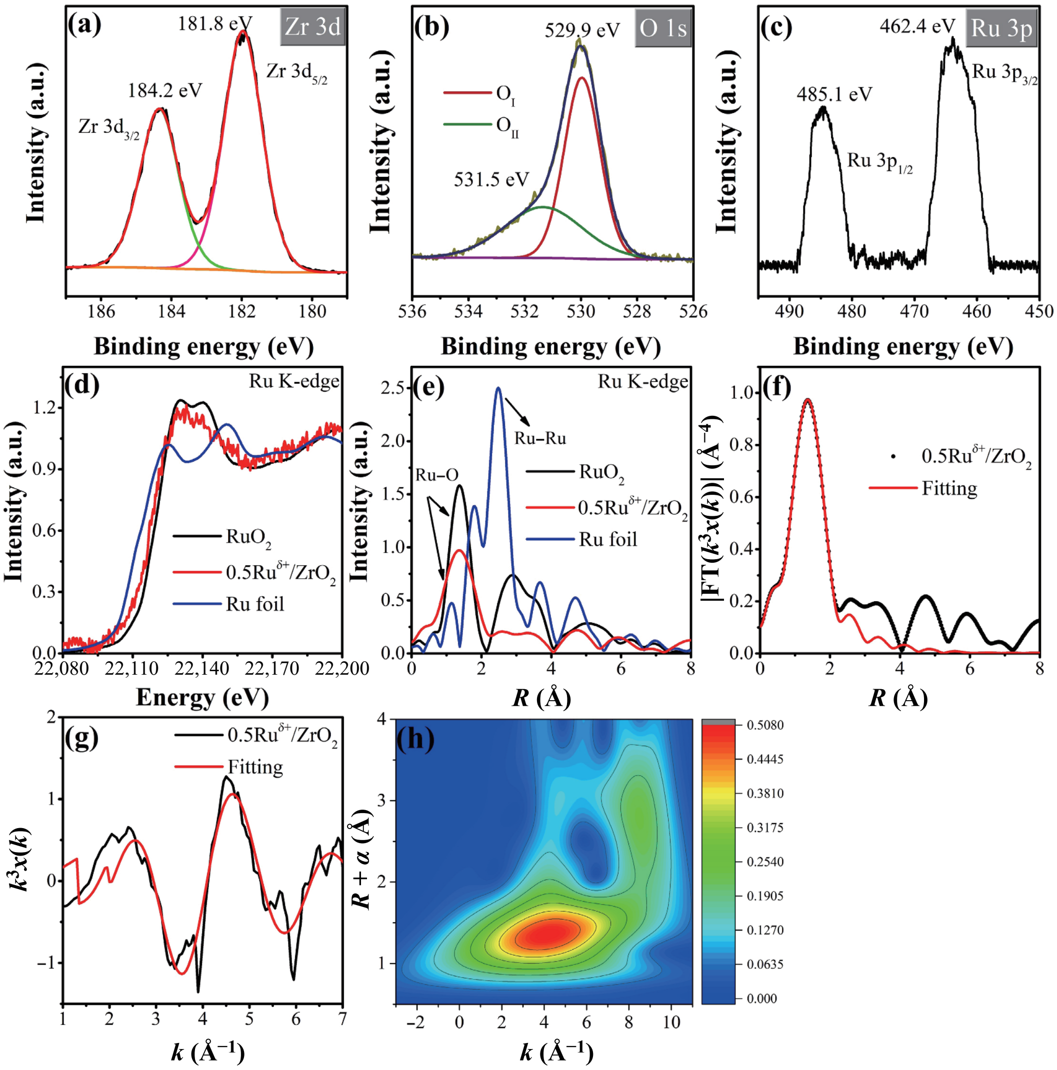

Figure 2 Characterization of the 0.5Ru$^{\delta+}$/ZrO$_2$ catalyst: XPS spectra of (a) Zr 3d, (b) O 1s, and (c) Ru 3p. (d) XANES, (e) EXAFS, (f) EXAFS R space fitting curve, (g) EXAFS k space fitting curve, and (h) EXAFS WT spectra.

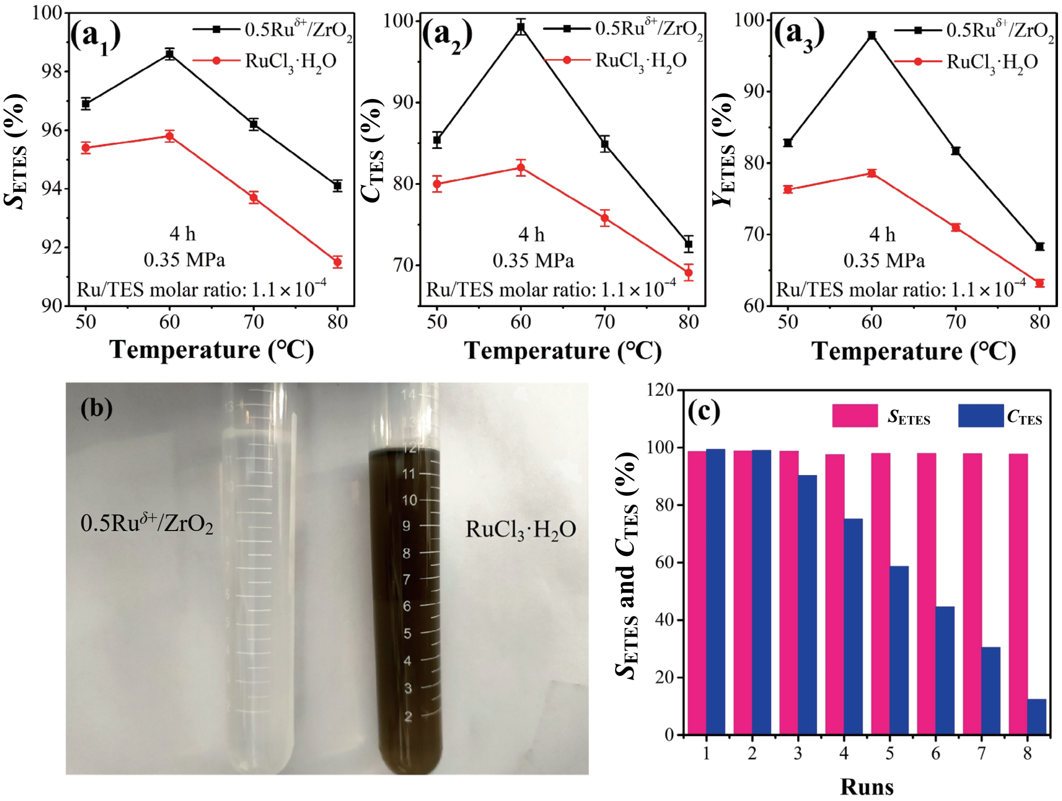

Figure 3 (a) Comparison of catalytic properties between 0.5Ru$^{\delta+}$/ZrO$_2$ and RuCl$_3$·H$_2$O under different reaction temperatures, (b) the product solution filtrated after reaction with 0.5Ru$^{\delta+}$/ZrO$_2$ catalyst (left) and homogeneous RuCl$_3$·H$_2$O catalyst (right), and (c) recycling performance of the 0.5Ru$^{\delta+}$/ZrO$_2$ catalyst.

the 0.5Ru$^{\delta+}$/ZrO$_2$ catalyst are much higher than those of RuCl$_3$·H$_2$O. The optimum reaction temperature for both heterogeneous and homogenous catalysts is 60 °C, at which the ETES selectivity and TES conversion on 0.5Ru$^{\delta+}$/ZrO$_2$ reach 98.6% and 99.3%, respectively, and 95.8% and 82.0% on RuCl$_3$·H$_2$O. However, when the reaction temperature is raised to 70 and 80 °C, both ETES selectivity and TES conversion on both catalysts are declined. It is well known that TES is very reactive and readily converted to byproduct TEOS at slightly high temperatures; therefore, the ETES selectivity decreases with increasing temperature [2]. In addition, the increased temperature leads to the significantly higher saturated vapor pressure of ethylene and less dissolution of ethylene in TES, and thus less participation of ethylene in the reaction, resulting in the decrease of TES.

We also investigated the effect of the pressure on the catalytic properties. Similarly, in the reaction pressure range of 0.0–0.7 MPa, 0.5Ru$^{\delta+}$/ZrO$_2$ shows a better catalytic performance in ETES selectivity (Fig. S4(a$_1$) in the ESM), TES conversion (Fig. S4(a$_2$) in the ESM), and ETES yield (Fig. S4(a$_3$) in the ESM) than RuCl$_3$·H$_2$O, and the optimum reaction pressure is 0.35 MPa, at which the dissolution rate and surface reaction rate of ethylene gas reach an equilibrium state. However, a further increase in pressure will not affect the TES conversion but will lower the ETES selectivity. It is because the excessive reaction pressure will lead to the disproportionation of TES and a decrease in ETES selectivity [55]. Similarly, in the reaction period of 1–6 h, 0.5Ru$^{\delta+}$/ZrO$_2$ exhibits better catalytic performance in ETES selectivity (Fig. S4(b$_1$) in the ESM), TES conversion (Fig. S4(b$_2$) in the ESM), and ETES yield (Fig. S4(b$_3$) in the ESM) than RuCl$_3$·H$_2$O, and the optimum reaction time is 4 h for 0.5Ru$^{\delta+}$/ZrO$_2$ and 3 h for RuCl$_3$·H$_2$O. Beyond their optimum reaction time, their ETES selectivities show a declining trend, although their TES conversions remain constant because a long reaction time can lead to the disproportionation of triethoxysilane [2]. Moreover, when the test is conducted in the Ru/TES molar ratio range of 3.7 × 10^{-5}–1.8 × 10^{-4}, 0.5Ru$^{\delta+}$/ZrO$_2$ also shows better catalytic performance than RuCl$_3$·H$_2$O in terms of ETES selectivity (Fig. S4(c$_1$) in the ESM), TES conversion (Fig. S4(c$_2$) in the ESM), and ETES yield (Fig. S4(c$_3$) in the ESM), and the optimum ratio is determined to be 1.1 × 10^{-4}. However, further increasing the molar ratio of Ru/TES will not enhance the conversion and selectivity.

Therefore, the hydrosilylation of TES with ethylene over the 0.5Ru$^{\delta+}$/ZrO$_2$ catalyst to produce ETES should be conducted at 60 °C, 0.35 MPa, and 4 h at the molar ratio of Ru/TES of 1.1 × 10^{-4}. Under this condition, the ETES selectivity and TES conversion are 98.6% and 99.3% for 0.5Ru$^{\delta+}$/ZrO$_2$, respectively, better than those of RuCl$_3$·3H$_2$O (97.0% and 95.9%) [2]. In addition, the calculated reaction activation energy of 0.5Ru$^{\delta+}$/ZrO$_2$ is 27.2 kJ/mol, which is much lower than that of the homogeneous catalyst RuCl$_3$·H$_2$O (53.4 kJ/mol) (see Figs. S5(a) and S5(b) in the ESM), proving that 0.5Ru$^{\delta+}$/ZrO$_2$ has a stronger ability to activate TES molecules. The turnover frequency (TOF) value of 0.5Ru$^{\delta+}$/ZrO$_2$ is calculated to be 1.02 s^{-1} (see Fig. S5(c) in the ESM). Additionally, using the same procedure, other Ru catalysts supported on different materials were synthesized, including 0.5Ru/CeO$_2$, 0.5Ru/Al$_2$O$_3$, and 0.5Ru/SiO$_2$, but all showed poorer catalytic properties compared to 0.5Ru$^{\delta+}$/ZrO$_2$ and RuCl$_3$·H$_2$O (Table S2 in the ESM), implying the unique property of ZrO$_2$ single nanocrystal. The XRD patterns of 0.5Ru/CeO$_2$, 0.5Ru/Al$_2$O$_3$, and 0.5Ru/SiO$_2$ in Fig. S6 in the ESM show there are no detectable diffraction peaks for the Ru species, and also no Ru crystal nanoparticles are observed in their TEM images (Fig. S7 in the ESM), possibly because the Ru species are dispersed on these supports in the form of atoms or clusters. It is known that the coordination environment for Ru SACs and the electronic interaction between Ru and different supports always result in different catalytic properties [56–60]. The full characterization and exploration of these catalysts will be conducted in our future work.

Figure 3(b) shows the product solution color after the hydrosilylation reaction with 0.5Ru$^{\delta+}$/ZrO$_2$ catalyst filtrated (left) and homogeneous $RuCl_3{\cdot}H_2O$ catalyst (right). The product solution is transparent or colorless after recovering the heterogeneous $0.5Ru^{\delta+}/ZrO_2$ catalyst by filtration. In contrast, when using $RuCl_3{\cdot}H_2O$ as the catalyst, the product solution shows a uniformly brown color, which would lead to difficulty in the product purification and separation process. Figure 3(c) shows the recycling performance of $0.5Ru^{\delta+}/ZrO_2$. There is almost no change in catalytic performance for ETES selectivity and TES conversion in the first two runs. After the sixth cycle, the ETES selectivity remains above 98.0%, but the TES conversion decreases from 99.3% in the first run to 12.4% in the eighth run.

We characterized this catalyst after the eighth run using TEM and found some sol-gel-like solid precipitates among ZrO_2 nanocrystals, but there was no observance of any Ru nanoparticles (Fig. S8(a) in the ESM). The elemental mapping image of $0.5Ru^{\delta+}/ZrO_2$ in Fig. S8(b) in the ESM further confirms the presence of Zr (Fig. S8(b_2) in the ESM), O (Fig. S8(b_3) in the ESM), and Ru (Fig. S8(b_4) in the ESM) species and Si-containing compounds (Fig. S8(b_5) in the ESM) on the ZrO_2 surface. It is well known that siloxanes are always used in preparing various silica materials via the hydrolysis process [61, 62]. We believe that after exposure to the air containing moisture, the siloxanes, including TES, ETES, and TEOS, present on the surface of $0.5Ru^{\delta+}/ZrO_2$, are easily hydrolyzed and further converted to sol-gel-like solid SiO_2, which may block the part of Ru single atom active sites, leading to a decline in TES conversion after several runs. This result suggests that our developed $0.5Ru^{\delta+}/ZrO_2$ catalyst should possess better reusability if it is not in contact with moisture during the separation and recycling stage.

3.3 Catalytic mechanism

DFT calculations were carried out to investigate the reaction mechanism of alkene hydrosilylation. The $0.5Ru^{\delta+}/ZrO_2$ model was established by supporting Ru single atoms on the ZrO_2 (111) surface (Fig. 4(a)). In $0.5Ru^{\delta+}/ZrO_2$, the Ru atom is located at a hollow site and connected to two 2-fold coordinated O atoms, with bond lengths of 1.99 and 2.09 Å, which are consistent with the EXAFS results. The distances between Ru and Zr atoms are 2.65 and 2.80 Å, respectively. According to Bader charge analysis, the calculated adsorption energy of Ru to the ZrO_2 (111) surface is −2.60 eV, with a positive charge of +0.48 |e|. Figure 4(b) shows that the electron density between Ru and Zr atoms increases, while the electron density between Ru and O atoms decreases. The increased charge density between Ru and Zr atoms implies that the Zr atoms on the surface play an important role in binding to the Ru single atom.

The reaction mechanism of alkene hydrosilylation on $0.5Ru^{\delta+}/ZrO_2$ is illustrated in Fig. 4(c). First, $SiH(OMe)_3$ is adsorbed on the active Ru single atom with an adsorption energy of −2.61 eV. The Si–H oxidative addition to Ru and formed intermediate H-Ru-Si $(OMe)_3$ has a very low barrier of 0.03 eV (TS1) and is exothermic by −1.38 eV. Subsequently, C_2H_4 co-adsorbed with H-Ru-Si $(OMe)_3$ on the Ru atom through p bonding with an adsorption energy of −1.58 eV. There are two pathways for C_2H_4 insertion: the typical Chalk–Harrod mechanism and the modified Chalk–Harrod mechanism [27, 63]. For the former mechanism (blue lines in Fig. 4(c)), C_2H_4 inserts into the Ru–H bond first, with a low barrier of 0.37 eV (TS2). After C_2H_5 formation, the next Si–C reductive elimination step has a barrier of 1.68 eV (TS3) and is endothermic by 1.14 eV. However, in the latter mechanism (red lines in Fig. 4(c)), C_2H_4 inserts into the Ru–Si bond first with a high barrier of 2.56 eV (TS4), which is much higher than the barrier of the Si–C reductive elimination step in the typical Chalk–Harrod mechanism. Therefore, our results demonstrate that the typical Chalk–Harrod mechanism is more favorable on the $0.5Ru^{\delta+}/ZrO_2$ catalyst, and the Si–C reductive elimination step is the rate-determining step of the whole reaction.

Based on the density functional theory calculations, the typical Chalke–Harrod mechanism, which is compatible with the experimental data, is proposed in Fig. 4(d). First, the intermediate H-Ru-Si$(OEt)_3$ is formed by the combination of TES [$HSi(OEt)_3$] and the active Ru species. Subsequently, the coordination of ethylene with Ru leads to the generation of an ethylene complex of Et-Ru-Si$(OEt)_3$, and ethylene is later further inserted between H and Ru atoms through the typical Chalke–Harrod mechanism. Finally, the product of $EtSi(OEt)_3$ is obtained when the active Ru species drop out via Si–C reductive elimination and are recycled in the hydrosilylation reaction. In the whole catalytic reaction, Si–C reductive elimination is the rate-determining step. For our $0.5Ru^{\delta+}/ZrO_2$, the atomic dispersion of active Ru species and the unique charge number of Ru single atoms play a key role in reducing the activation energy of this step.

4 Conclusions

In summary, we have developed a heterogeneous Ru-based catalyst consisting of partially charged single-atom Ru supported

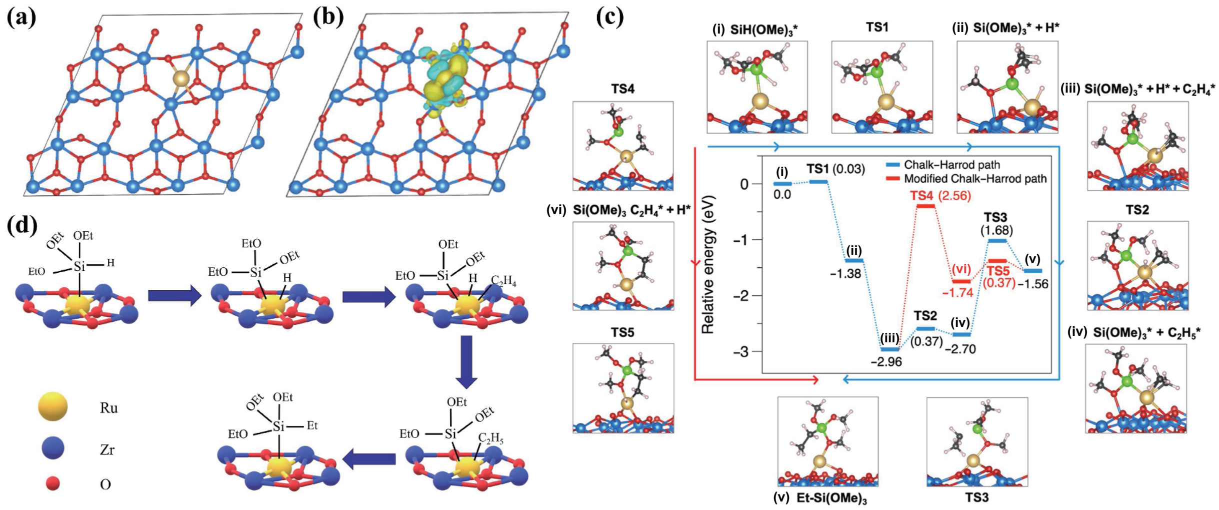

Figure 4 (a) Optimized structures and (b) charge density differences of $0.5Ru^{\delta+}/ZrO_2$. Blue and yellow areas represent charge reduction and increase, respectively. The cut-off of the density-difference iso-surfaces is equal to 0.004 electrons/Å^3 (Zr: blue, O: red, and Ru: gold). (c) Reaction pathway for alkene hydrosilylation on $0.5Ru^{\delta+}/ZrO_2$. The inset shows the potential energy diagram, and numbers in parentheses indicate the barriers of elementary steps (Ru: gold, Si: green, Zr: blue, O: red, C: black, and H: white). (d) Proposed Chalk–Harrod mechanism for the hydrosilylation of TES with ethylene catalyzed by $0.5Ru^{\delta+}/ZrO_2$.

on ZrO_2 nanocrystals (0.5$Ru^{\delta+}/ZrO_2$), exhibiting remarkable activity, optimal selectivity, and reusability in the ethylene hydrosilylation with TES, superior to the traditional and industrial homogeneous catalyst ($RuCl_3{\cdot}H_2O$). The unusual catalytic property of 0.5$Ru^{\delta+}/ZrO_2$ can be attributed to the unique partially positive-charged electronic structure and atomic dispersion of the Ru species. The preparation of this catalyst does not involve complicated procedures, any toxic or expensive chemicals, and harsh treatment conditions, allowing for easy industrial manufacture. Applying this single-atom 0.5$Ru^{\delta+}/ZrO_2$ catalyst realizes both the high atom utilization and the recyclability of Ru, making it possible for a greener industrial hydrosilylation process to replace the present homogeneous catalytic process.

Acknowledgements

This work was supported by the National Natural Science Foundation of China (No. 22002004). Y. J. J. thanks the financial supports from the Outstanding Youth Cultivation Program of Beijing Technology and Business University (No. 19008021144), and Research Foundation for Advanced Talents of Beijing Technology and Business University (No. 19008020159). Z. Y. Z. thanks the financial support of Guangdong Key discipline fund for this collaboration.

Electronic Supplementary Material: Supplementary material (TG curve, H_2-TPR profile, XRD patterns and H_2-TPD profile of the 0.5$Ru^{\delta+}/ZrO_2$ and ZrO_2, SEM of ZrO_2, other catalytic performance, the calculated reaction activation energy of 0.5$Ru^{\delta+}/ZrO_2$, the calculated reaction activation energy of 0.5$Ru^{\delta+}/ZrO_2$ and $RuCl_3{\cdot}H_2O$, XRD patterns and TEM images of the catalysts with different support, and TEM images of the 0.5$Ru^{\delta+}/ZrO_2$ catalyst after the eighth run) is available in the online version of this article at https://doi.org/10.1007/s12274-022-4227-4.

References

[1] Marciniec, B. Catalysis by transition metal complexes of alkene silylation-recent progress and mechanistic implications. *Coord. Chem. Rev.* **2005**, *249*, 2374–2390.

[2] Liu, L.; Li, X. N.; Dong, H.; Wu, C. Hydrosilylation reaction of ethylene with triethoxysilane catalyzed by ruthenium halides and promoted by cuprous halides. *J. Organomet. Chem.* **2013**, *745–746*, 454–459.

[3] Nakajima, Y.; Shimada, S. Hydrosilylation reaction of olefins: Recent advances and perspectives. *RSC Adv.* **2015**, *5*, 20603–20616.

[4] Speier, J. L.; Webster, J. A.; Barnes, G. H. The addition of silicon hydrides to olefinic double bonds. Part II. The use of group VIII metal catalysts. *J. Am. Chem. Soc.* **1957**, *79*, 974–979.

[5] Karstedt, B. Platinum complexes of unsaturated siloxanes and platinum containing organopolysiloxanes. U. S. Patent 3, 775, 452, November 27, 1973.

[6] Hilal, H. S.; Khalaf, S.; Jondi, W. Cluster versus non-cluster catalysis in olefin thermal isomerization and hydrosilylation in the presence of $Ru_3(CO)_{12}$. *J. Organomet. Chem.* **1993**, *452*, 167–173.

[7] Tanaka, M.; Hayashi, T.; Mi, Z. Y. Ruthenium complex-catalyzed hydrosilylation of allyl chloride with trimethoxysilane. *J. Mol. Catal.* **1993**, *81*, 207–214.

[8] Chalk, A. J. The hydrosilation of olefins catalzed by some rhodium and cobalt complexes. *J. Organomet. Chem.* **1970**, *21*, 207–213.

[9] Tondreau, A. M.; Atienza, C. C. H.; Weller, K. J.; Nye, S. A.; Lewis, K. M.; Delis, J. G. P.; Chirik, P. J. Iron catalysts for selective anti-Markovnikov alkene hydrosilylation using tertiary silanes. *Science* **2012**, *335*, 567–570.

[10] Marko´, I. E.; Ste´rin, S.; Buisine, O.; Mignani, G.; Branlard, P.; Tinant, B.; Declercq, J. P. Selective and efficient platinum(0)-carbene complexes as hydrosilylation catalysts. *Science* **2002**, *298*, 204–206.

[11] Ciriminna, R.; Pandarus, V.; Gingras, G.; Béland, F.; Pagliaro, M. Closing the organosilicon synthetic cycle: Efficient heterogeneous hydrosilylation of alkenes over Silia*Cat* Pt(0). *ACS Sustainable Chem. Eng.* **2013**, *1*, 249–253.

[12] Jawale, D. V.; Geertsen, V.; Miserque, F.; Berthault, P.; Gravel, E.; Doris, E. Solvent-free hydrosilylation of alkenes and alkynes using recyclable platinum on carbon nanotubes. *Green Chem.* **2021**, *23*, 815–820.

[13] Bandari, R.; Buchmeiser, M. R. Polymeric monolith supported Pt-nanoparticles as ligand-free catalysts for olefinhydrosilylation under batch and continuous conditions. *Catal. Sci. Technol.* **2012**, *2*, 220–226.

[14] Polizzi, C.; Caporusso, A. M.; Vitulli, G.; Salvadori, P.; Pasero, M. Supported platinum atoms derived catalysts in the hydrosilylation of unsaturated substrates. *J. Mol. Catal.* **1994**, *91*, 83–90.

[15] Marciniec, B.; Maciejewski, H.; Duczmal, W.; Fiedorow, R.; Kityński, D. Kinetics and mechanism of the reaction of allyl chloride with trichlorosilane catalyzed by carbon-supported platinum. *Appl. Organomet. Chem.* **2003**, *17*, 127–134.

[16] Jiang, Y. N.; Zeng, J. H.; Yang, Y.; Liu, Z. K.; Chen, J. J.; Li, D. C.; Chen, L.; Zhan, Z. P. A conjugated microporous polymer as a recyclable heterogeneous ligand for highly efficient regioselective hydrosilylation of allenes. *Chem. Commun.* **2020**, *56*, 1597–1600.

[17] Chauhan, M.; Hauck, B. J.; Keller, L. P.; Boudjouk, P. Hydrosilylation of alkynes catalyzed by platinum on carbon. *J. Organomet. Chem.* **2002**, *645*, 1–3.

[18] Jiménez, R.; López, J. M.; Cervantes, J. Metal supported catalysts obtained by sol-gel in the hydrosilylation of phenylacetylene with R_3SiH organosilanes (R_3 = Ph_3, Ph_2Me, and $PhMe_2$). *Can. J. Chem.* **2000**, *78*, 1491–1495.

[19] Zhang, N. Q.; Ye, C. L.; Yan, H.; Li, L. C.; He, H.; Wang, D. S.; Li, Y. D. Single-atom site catalysts for environmental catalysis. *Nano Res.* **2020**, *13*, 3165–3182.

[20] Zhang, J.; Zheng, C. Y.; Zhang, M. L.; Qiu, Y. J.; Xu, Q.; Cheong, W. C.; Chen, W. X.; Zheng, L. R.; Gu, L.; Hu, Z. P. et al. Controlling N-doping type in carbon to boost single-atom site Cu catalyzed transfer hydrogenation of quinoline. *Nano Res.* **2020**, *13*, 3082–3087.

[21] Li, W. H.; Yang, J. R.; Wang, D. S.; Li, Y. D. Striding the threshold of an atom era of organic synthesis by single-atom catalysis. *Chem* **2022**, *8*, 119–140.

[22] Gao, P.; Liang, G. F.; Ru, T.; Liu, X. Y.; Qi, H. F.; Wang, A. Q.; Chen, F. E. Phosphorus coordinated Rh single-atom sites on nanodiamond as highly regioselective catalyst for hydroformylation of olefins. *Nat. Commun.* **2021**, *12*, 4698.

[23] Xiong, Y.; Sun, W. M.; Han, Y. H.; Xin, P. Y.; Zheng, X. S.; Yan, W. S.; Dong, J. C.; Zhang, J.; Wang, D. S.; Li, Y. D. Cobalt single atom site catalysts with ultrahigh metal loading for enhanced aerobic oxidation of ethylbenzene. *Nano Res.* **2021**, *14*, 2418–2423.

[24] Lang, R.; Li, T. B.; Matsumura, D.; Miao, S.; Ren, Y. J.; Cui, Y. T.; Tan, Y.; Qiao, B. T.; Li, L.; Wang, A. Q. et al. Hydroformylation of olefins by a rhodium single-atom catalyst with activity comparable to $RhCl(PPh_3)_3$. *Angew. Chem., Int. Ed.* **2016**, *55*, 16054–16058.

[25] Mori, K.; Taga, T.; Yamashita, H. Isolated single-atomic Ru catalyst bound on a layered double hydroxide for hydrogenation of CO_2 to formic acid. *ACS Catal.* **2017**, *7*, 3147–3151.

[26] Zai, H. C.; Zhao, Y. Z.; Chen, S. Y.; Ge, L.; Chen, C. F.; Chen, Q.; Li, Y. J. Heterogeneously supported pseudo-single atom Pt as sustainable hydrosilylation catalyst. *Nano Res.* **2018**, *11*, 2544–2552.

[27] Chen, Y. J.; Ji, S. F.; Sun, W. M.; Chen, W. X.; Dong, J. C.; Wen, J. F.; Zhang, J.; Li, Z.; Zheng, L. R.; Chen, C. et al. Discovering partially charged single-atom Pt for enhanced anti-markovnikov alkene hydrosilylation. *J. Am. Chem. Soc.* **2018**, *140*, 7407–7410.

[28] Cui, X. J.; Junge, K.; Dai, X. C.; Kreyenschulte, C.; Pohl, M. M.; Wohlrab, S.; Shi, F.; Brückner, A.; Beller, M. Synthesis of single atom based heterogeneous platinum catalysts: High selectivity and activity for hydrosilylation reactions. *ACS Cent. Sci.* **2017**, *3*, 580–585.

[29] Xiao, M. L.; Gao, L. Q.; Wang, Y.; Wang, X.; Zhu, J. B.; Jin, Z.; Liu, C. P.; Chen, H. Q.; Li, G. R.; Ge, J. J. et al. Engineering energy level of metal center: Ru single-atom site for efficient and durable

oxygen reduction catalysis. *J. Am. Chem. Soc.* **2019**, *141*, 19800–19806.

[30] Wang, J.; Fang, W. H.; Hu, Y.; Zhang, Y. H.; Dang, J. Q.; Wu, Y.; Chen, B. Z.; Zhao, H.; Li, Z. X. Single atom Ru doping 2H-MoS_2 as highly efficient hydrogen evolution reaction electrocatalyst in a wide pH range. *Appl. Catal. B* **2021**, *298*, 120490.

[31] Wang, X. Y.; Li, L. L.; Fang, Z. P.; Zhang, Y. F.; Ni, J.; Lin, B. Y.; Zheng, L. R.; Au, C. T.; Jiang, L. L. Atomically dispersed Ru catalyst for low-temperature nitrogen activation to ammonia via an associative mechanism. *ACS Catal.* **2020**, *10*, 9504–9514.

[32] Li, X. Y.; Han, Y. J.; Huang, Y. K.; Lin, J.; Pan, X. L.; Zhao, Z.; Zhou, Y. L.; Wang, H.; Yang, X. F.; Wang, A. Q. et al. Hydrogenated TiO_2 supported Ru for selective methanation of CO in practical conditions. *Appl. Catal. B* **2021**, *298*, 120597.

[33] Wang, X.; Chen, W. X.; Zhang, L.; Yao, T.; Liu, W.; Lin, Y.; Ju, H. X.; Dong, J. C.; Zheng, L. R.; Yan, W. S. et al. Uncoordinated amine groups of metal-organic frameworks to anchor single Ru sites as chemoselective catalysts toward the hydrogenation of quinoline. *J. Am. Chem. Soc.* **2017**, *139*, 9419–9422.

[34] Jing, Y. X.; Wang, Y. Q.; Furukawa, S.; Xia, J.; Sun, C. Y.; Hülsey, M. J.; Wang, H. F.; Guo, Y.; Liu, X. H.; Yan, N. Towards the circular economy: Converting aromatic plastic waste back to arenes over a Ru/Nb_2O_5 catalyst. *Angew. Chem., Int. Ed.* **2021**, *60*, 5527–5535.

[35] Zhu, Y. Q.; Cao, T.; Cao, C. B.; Luo, J.; Chen, W. X.; Zheng, L. R.; Dong, J. C.; Zhang, J.; Han, Y. H.; Li, Z. et al. One-pot pyrolysis to N-doped graphene with high-density Pt single atomic sites as heterogeneous catalyst for alkene hydrosilylation. *ACS Catal.* **2018**, *8*, 10004–10011.

[36] Ravel, B.; Newville, M. *ATHENA, ARTEMIS, HEPHAESTUS*: Data analysis for X-ray absorption spectroscopy using IFEFFIT. *J. Synchrotron Radiat.* **2005**, *12*, 537–541.

[37] Kresse, G.; Furthmüller, J. Efficiency of *ab-initio* total energy calculations for metals and semiconductors using a plane-wave basis set. *Comput. Mater. Sci.* **1996**, *6*, 15–50.

[38] Kresse, G.; Furthmüller, J. Efficient iterative schemes for *ab initio* total-energy calculations using a plane-wave basis set. *Phys. Rev. B* **1996**, *54*, 11169–11186.

[39] Kresse, G.; Joubert, D. From ultrasoft pseudopotentials to the projector augmented-wave method. *Phys. Rev. B* **1999**, *59*, 1758–1775.

[40] Perdew, J. P.; Burke, K.; Ernzerhof, M. Generalized gradient approximation made simple. *Phys. Rev. Lett.* **1996**, *77*, 3865–3868.

[41] Dudarev, S. L.; Botton, G. A.; Savrasov, S. Y.; Humphreys, C. J.; Sutton, A. P. Electron-energy-loss spectra and the structural stability of nickel oxide: An LSDA + *U* study. *Phys. Rev. B* **1998**, *57*, 1505–1509.

[42] Anisimov, V. I.; Aryasetiawan, F.; Lichtenstein, A. I. First-principles calculations of the electronic structure and spectra of strongly correlated systems: The LDA + *U* method. *J. Phys. :Condens. Matter* **1997**, *9*, 767–808.

[43] Tang, Y.; Zhao, S.; Long, B.; Liu, J. C.; Li, J. On the nature of support effects of metal dioxides MO_2 (M = Ti, Zr, Hf, Ce, Th) in single-atom gold catalysts: Importance of quantum primogenic effect. *J. Phys. Chem. C* **2016**, *120*, 17514–17526.

[44] Jónsson, H.; Mills, G.; Jacobsen, K. W. Nudged elastic band method for finding minimum energy paths of transitions. In *Classical and Quantum Dynamics in Condensed Phase Simulations*. Berne, B. J., Ed.; Sinqapore: World Scientific, 1998; pp 385–404.

[45] Henkelman, G.; Uberuaga, B. P.; Jónsson, H. A climbing image nudged elastic band method for finding saddle points and minimum energy paths. *J. Chem. Phys.* **2000**, *113*, 9901–9904.

[46] Henkelman, G.; Jónsson, H. Improved tangent estimate in the nudged elastic band method for finding minimum energy paths and saddle points. *J. Chem. Phys.* **2000**, *113*, 9978–9985.

[47] Tao, H. C.; Choi, C.; Ding, L. X.; Jiang, Z.; Han, Z. S.; Jia, M. W.; Fan, Q.; Gao, Y. N.; Wang, H. H.; Robertson, A. W. et al. Nitrogen fixation by Ru single-atom electrocatalytic reduction. *Chem* **2019**, *5*, 204–214.

[48] Ftouni, J.; Muñoz-Murillo, A.; Goryachev, A.; Hofmann, J. P.; Hensen, E. J. M.; Lu, L.; Kiely, C. J.; Bruijnincx, P. C. A.; Weckhuysen, B. M. ZrO_2 Is preferred over TiO_2 as support for the Ru-catalyzed hydrogenation of levulinic acid to γ-valerolactone. *ACS Catal.* **2016**, *6*, 5462–5472.

[49] Hernández, W. Y.; Centeno, M. A.; Ivanova, S.; Eloy, P.; Gaigneaux, E. M.; Odriozola, J. A. Cu-modified cryptomelane oxide as active catalyst for CO oxidation reactions. *Appl. Catal. B* **2012**, *123*–124, 27–35.

[50] Mo, S. P.; Li, S. D.; Li, W. H.; Li, J. Q.; Chen, J. Y.; Chen, Y. F. Excellent low temperature performance for total benzene oxidation over mesoporous CoMnAl composited oxides from hydrotalcites. *J. Mater. Chem. A* **2016**, *4*, 8113–8122.

[51] Bian, Z. F.; Chan, Y. M.; Yu, Y.; Kawi, S. Morphology dependence of catalytic properties of Ni/CeO_2 for CO_2 methanation: A kinetic and mechanism study. *Catal. Today* **2020**, *347*, 31–38.

[52] Wang, J.; Wei, Z. Z.; Mao, S. J.; Li, H. R.; Wang, Y. Highly uniform Ru nanoparticles over N-doped carbon: pH and temperature-universal hydrogen release from water reduction. *Energy Environ. Sci.* **2018**, *11*, 800–806.

[53] Funke, H.; Scheinost, A. C.; Chukalina, M. Wavelet analysis of extended x-ray absorption fine structure data. *Phys. Rev. B* **2005**, *71*, 094110.

[54] Wang, S. Z.; Zhang, K. L.; Li, H. L.; Xiao, L. P.; Song, G. Y. Selective hydrogenolysis of catechyl lignin into propenylcatechol over an atomically dispersed ruthenium catalyst. *Nat. Commun.* **2021**, *12*, 416.

[55] Liu, L.; Li, X.; Ma, Y.; Wu, C.; Han, G. Selective catalytic hydrosilylation of ethylene. Preparation of ethyltrimethoxysilane by H_2O promoted $RuCl_3{\cdot}3H_2O$ catalyst. *Kinet. Catal.* **2020**, *61*, 414–420.

[56] Wang, Y.; Zheng, X. B.; Wang, D. S. Design concept for electrocatalysts. *Nano Res.* **2022**, *15*, 1730–1752.

[57] Su, P. P.; Pei, W.; Wang, X. W.; Ma, Y. F.; Jiang, Q. K.; Liang, J.; Zhou, S.; Zhao, J. J.; Liu, J.; Lu, G. Q. Exceptional electrochemical HER performance with enhanced electron transfer between Ru nanoparticles and single atoms dispersed on a carbon substrate. *Angew. Chem., Int. Ed.* **2021**, *60*, 16044–16050.

[58] Boyjoo, Y.; Wang, M. W.; Pareek, V. K.; Liu, J.; Jaroniec, M. Synthesis and applications of porous non-silica metal oxide submicrospheres. *Chem. Soc. Rev.* **2016**, *45*, 6013–6047.

[59] Liu, X. Y.; Ye, S.; Lan, G. J.; Su, P. P.; Zhang, X. L.; Price, C. A. H.; Li, Y.; Liu, J. Atomic pyridinic nitrogen sites promoting levulinic acid hydrogenations over double-shelled hollow Ru/C nanoreactors. *Small* **2021**, *17*, 2101271.

[60] Jing, H. Y.; Zhu, P.; Zheng, X. B.; Zhang, Z. D.; Wang, D. S.; Li, Y. D. Theory-oriented screening and discovery of advanced energy transformation materials in electrocatalysis. *Adv. Powder Mater.*, in press, DOI: 10.1016/j.apmate.2021.10.004.

[61] Osseo-Asare, K.; Arriagada, F. J. Preparation of SiO_2 nanoparticles in a non-ionic reverse micellar system. *Colloids Surf.* **1990**, *50*, 321–339.

[62] Stöber, W.; Fink, A.; Bohn, E. Controlled growth of monodisperse silica spheres in the micron size range. *J. Colloid Interface Sci.* **1968**, *26*, 62–69.

[63] Chalk, A. J.; Harrod, J. F. Reactions between dicobalt octacarbonyl and silicon hydrides. *J. Am. Chem. Soc.* **1965**, *87*, 1133–1135.